IEEE Access
Multidisciplinary ⋮ Rapid Review ⋮ Open Access Journal

Received March 31, 2022, accepted April 11, 2022, date of publication April 18, 2022, date of current version April 27, 2022.

Digital Object Identifier 10.1109/ACCESS.2022.3168390

An Adjustable Wide-Range Speed-Control Method for Sensorless IPMSM Drive Systems

MUHAMMAD SYAHRIL MUBAROK, (Graduate Student Member, IEEE), AND TIAN-HUA LIU, (Life Fellow, IEEE)

Department of Electrical Engineering, National Taiwan University of Science and Technology, Taipei 106, Taiwan

Corresponding author: Tian-Hua Liu (liu@mail.ntust.edu.tw)

This work was supported by the Ministry of Science and Technology (MOST), Taiwan, under Grant MOST 110-2221-E-011-086.

ABSTRACT This paper proposes an adjustable wide-range speed-control method for sensorless IPMSM drive systems from standstill, low-speeds, middle-speeds, and high-speeds in the flux-weakening region. A sensorless method and an online parameter estimation method based on the measurement of current-slope under SVPWM with an extension compensation are proposed. The estimated rotor position, rotor speed, *d-q* axis inductances, magnetic flux, and torque of the IPMSM are precisely computed by using a current-slope measurement, and then a closed-loop speed control sensorless IPMSM drive system is implemented without requiring any external high-frequency signal injection or a complicated observer. In addition, to achieve a high-performance sensorless IPMSM drive system, the estimated parameters are used for real-time maximum torque per ampere control and flux-weakening control. Finally, the proposed sensorless IPMSM drive system provides a wide operation range from 1 r/min to 3000 r/min with excellent performance in constant-torque regions and flux-weakening regions. A digital signal processor, made by Texas Instrument, type TMS 320F2802, is employed to realize the control algorithm and estimation algorithm. Experimental results show the proposed sensorless IPMSM drive system achieves satisfactory responses, including $\pm 2.5°$ of electrical position estimation errors, good dynamic responses, and good tracking responses.

INDEX TERMS Current-slope measurement, sensorless drive, online parameter estimation, maximum torque per ampere control, flux-weakening control, IPMSM.

I. INTRODUCTION

Interior permanent magnet synchronous motors (IPMSM) have been used in different industrial applications, such as electric vehicles, elevators, and robots due to their superior performance in terms of high-power density, high efficiency, good robustness, and wide-speed operation ranges [1], [2].

These sensorless IPMSM drives have been investigated for more than four decades. Generally speaking, the sensorless techniques are classified into four major categories: high-frequency voltage or high-frequency current injection methods [3], [4], extended back electromotive force (back-EMF) methods [5], [6], indirect flux detection methods [7], [8], and fundamental pulse-width modulation (PWM) current-slope methods. The fundamental PWM method, which is the most popular, uses current-slope detection based on space-vector pulse width modulation (SVPWM) in each switching interval. By using the current-slope of the fundamental SVPWM, the estimated rotor position was precisely obtained [9], [10]. The advantage of this method was that it could be used in a wide speed range. However, a current-slope detection method was required to comply with the minimum time duration to precisely acquire the estimated rotor position. As a result, a cramped voltage vector was required to extend the minimum duration. Then, a compensation vector was therefore required [11], [12]. In [13], an optimized asymmetric PWM was proposed to obtain longer active voltage vectors and more accurate current-slope measurements. However, the position estimation errors were within $\pm 9^0$, which could be too large.

These sensorless methods required measurements of the motor parameters. In fact, the real parameters are varied due to magnetic saturation and temperature changes. As a result, the difference between the real position and estimated position had large estimation errors as the motor parameter variations are too great in sensorless methods [14]. To overcome this problem, several online parameter estimation methods based on sensorless drives have been proposed by several researchers [15]–[21]. For example, Ichikawa *et al.* [15]

The associate editor coordinating the review of this manuscript and approving it for publication was Shihong Ding.

investigated an extended back electromotive force sensorless method with online parameter identification where the recursive least-square (RLS) method was employed. The resistance and *d*-*q* axis inductances were estimated and were not influenced by the position error under sensorless control. As a result, the sensorless drive with identified parameters could maintain good position estimation accuracy. Piippo *et al.* [16] investigated an adaptive observer with a high-frequency signal injection sensorless method, in which an observer was used for the parameter estimation. The stator resistance was estimated at low speed from an error signal that was produced by the injecting signal. The permanent magnet flux was estimated at medium to high speeds from the *d*-axis current estimation errors. Inoue *et al.* [17] investigated a model-based sensorless method with online parameter estimation using the RLS method. The resistance was identified online; however, the *q*-axis inductance was identified off-line. The identified resistance in the sensorless drive system improved the accuracy of the estimated position in low speed regions. Hamida *et al.* [18] investigated an adaptive interconnected observer for rotor speed, rotor position, load torque, stator inductance, and stator resistance estimations. However, the estimated position error produced by that method was within 0.18 rad, which was too large, and the proposed observer was also complicated. Rafaq *et al.* [19] investigated an online parameter identification method based on an affine projection algorithm to estimate the stator resistance and *d*-*q* axis stator inductances for model-based sensorless control. The online updated parameter made the sensorless method stable and robust while the motor parameters varied. However, the estimated position error, which was near 0.2 rad, was relatively large. Yao *et al.* [20] investigated online parameter estimation based on adaptive full-state feedback current control for back-EMF sensorless drives. The performance of the sensorless drives were improved since online parameters were implemented at medium-speeds to high-speeds. However. The estimated position errors at medium-speeds deteriorated to $\pm 4°$. Tang *et al.* [21] investigated a rotor-flux-model-based sensorless maximum torque per ampere (MTPA) control for IPMSMs by estimating a virtual *q*-axis inductance that was obtained by using a virtual high-frequency injecting signal. Simple signal processing was used to acquire the virtual *q*-axis inductance in real time. Furthermore, an effective range, based on the nominal inductance, was used. As a result, a sensorless MTPA control operation was achieved in a limited range. However, the estimated position errors were near $\pm 6°$, which was too large.

In previous papers [15]–[21], the sensorless and online parameter estimation methods were separated, and this increased the complexity in their implemented drive system and also aggravated the computational burden. In this paper, a sensorless drive system including rotor position and online parameter estimation methods based on current-slope measurements is investigated. The current-slope is computed in each switching state during a sampling interval by measuring two points of the stator currents. After that, the rotor position, rotor speed, *d*-*q* axis inductances, magnetic flux, and torque of the IPMSM are precisely estimated. The proposed online parameter estimation is obtained when the DSP executes the sensorless method. As a result, we can implement a simple method without requiring any external high-frequency signal injections or complicated observers. To achieve a high-performance sensorless IPMSM drive system, the estimated parameters are used for real-time MTPA and flux-weakening control. Finally, experimental results show that the proposed sensorless IPMSM drive system provides a wide operation range from 1 r/min to 3000 r/min with excellent performance in the constant-torque and flux-weakening regions. The performance in this paper is better than that in previously published papers [15]–[21]. To the author's best knowledge, these two major points are original and are the main contributions of this paper.

II. SENSORLESS TECHNIQUE

A. IPMSM MODEL

The voltage equations of the IPMSM in the *a*-*b*-*c* stationary frame are described as follows:

$$\begin{bmatrix} v_a \\ v_b \\ v_c \end{bmatrix} = r_s \begin{bmatrix} i_a \\ i_b \\ i_c \end{bmatrix} + \frac{d}{dt}\left[\begin{bmatrix} i_a \\ i_b \\ i_c \end{bmatrix} \begin{bmatrix} L_{sa} & L_{mab} & L_{mac} \\ L_{mba} & L_{sb} & L_{mbc} \\ L_{mca} & L_{mcb} & L_{sc} \end{bmatrix} + \lambda_m \begin{bmatrix} \cos\theta_e \\ \cos\left(\theta_e - \frac{2\pi}{3}\right) \\ \cos\left(\theta_e + \frac{2\pi}{3}\right) \end{bmatrix} \right] \tag{1}$$

where v_a, v_b, and v_c are the three-phase voltages; r_s is the stator resistance; i_a, i_b, and i_c are the three-phase stator currents; d/dt is the differential operator; L_{sa}, L_{sb}, and L_{sc} are the three-phase self-inductances; $L_{mab}, L_{mac}, L_{mba}, L_{mbc}$, L_{mca}, and L_{mcb} are the three-phase mutual inductances;λ_m is the permanent-magnet flux; and θ_e is the electrical rotor position of the IPMSM. The three-phase self-inductances are shown as:

$$L_{sa} = L_l + L_x - L_y \cos(2\theta_e) \tag{2}$$

$$L_{sb} = L_l + L_x - L_y \cos(2\theta_e + \frac{2\pi}{3}) \tag{3}$$

and

$$L_{sc} = L_l + L_x - L_y \cos(2\theta_e - \frac{2\pi}{3}) \tag{4}$$

Furthermore, the three-phase mutual-inductances are described as:

$$L_{mab} = L_{mba} = -\frac{1}{2}L_x - L_y \cos(2\theta_e - \frac{2\pi}{3}) \tag{5}$$

$$L_{mbc} = L_{mcb} = -\frac{1}{2}L_x - L_y \cos(2\theta_e) \tag{6}$$

and

$$L_{mca} = L_{mac} = -\frac{1}{2}L_x - L_y \cos(2\theta_e + \frac{2\pi}{3}) \tag{7}$$

where L_l is the leakage inductance, L_x is the constant value parameter of the self-inductance and mutual inductance, and L_y is the varying parameter that is related to the cos $(2\theta_e)$ of the self-inductance and mutual inductance. The relationship between L_l, L_x, and L_y and L_d and L_q can be expressed as [22]

$$L_d = L_l + \frac{3}{2}\left(L_x - L_y\right) \tag{8}$$

and

$$L_q = L_l + \frac{3}{2}\left(L_x + L_y\right) \tag{9}$$

where L_d is the d-axis inductance and L_q is the q-axis inductance of the IPMSM. The total torque of the IPMSM is shown as follows:

$$T_e = \frac{3P}{4}\left[(L_d - L_q)i_d i_q + \lambda_m i_q\right] \tag{10}$$

where T_e is the total torque, P is the pole number, i_d is the d-axis current, and i_q is the q- axis current. The dynamic equation of the mechanical speed of the IPMSM can be expressed as:

$$\frac{d}{dt}\omega_m = \frac{1}{J_m}\left(T_e - T_L - B_m\omega_m\right) \tag{11}$$

where ω_m is the mechanical speed of the IPMSM, J_m is the inertia of the IPMSM, T_L is the external load, and B_m is the friction coefficient of the motor. The relationship between the mechanical speed and the electrical speed of the IPMSM is expressed as:

$$\omega_e = \frac{P}{2}\omega_m \tag{12}$$

where ω_e is the electrical speed of the IPMSM.

B. SVPWM-BASED CURRENT-SLOPE SENSORLESS TECHNIQUE

SVPWM is a very popular modulation technique for field-oriented control (FOC) for IPMSM drive systems. It provides a fixed switching state for each sector. The three switching states occur in one sector of a sampling interval and include two active voltage vectors and one zero voltage vector. Based on these principles, the rotor position estimation is derived by using the current-slope obtained from these three consecutive switching states.

Assuming that the vector position is in sector 1 and the three switching states V_1, V_2, and V_7 are used, the current-slopes are measured by detecting the two points of the stator currents which are generated by each voltage vector. By using this method, the relationships among the voltage vectors, switching states, and output voltages are shown in Table 1, in which each switching state generates an output voltage.

The voltage equations that use the first active voltage vector V_1 are expressed as follows:

$$0.67V_{dc} = r_s i_a + L_{sa}\frac{di_a^{V_1}}{dt} + L_{mab}\frac{di_b^{V_1}}{dt} + L_{mac}\frac{di_c^{V_1}}{dt} - \lambda_m\omega_e \sin\theta_e + \left[i_a\frac{dL_{sa}^{V_1}}{d\theta_e} + i_b\frac{dL_{mab}^{V_1}}{d\theta_e} + i_c\frac{dL_{mac}^{V_1}}{d\theta_e}\right]\omega_e \tag{13}$$

$$-0.33V_{dc} = r_s i_b + L_{mba}\frac{di_a^{V_1}}{dt} + L_{sb}\frac{di_b^{V_1}}{dt} + L_{mbc}\frac{di_c^{V_1}}{dt} - \lambda_m\omega_e \sin\left(\theta_e - \frac{2\pi}{3}\right) + \left[i_a\frac{dL_{mba}^{V_1}}{d\theta_e} + i_b\frac{dL_{sb}^{V_1}}{d\theta_e} + i_c\frac{dL_{mbc}^{V_1}}{d\theta_e}\right]\omega_e \tag{14}$$

and

$$-0.33V_{dc} = r_s i_c + L_{mca}\frac{di_a^{V_1}}{dt} + L_{mcb}\frac{di_b^{V_1}}{dt} + L_{sc}\frac{di_c^{V_1}}{dt} - \lambda_m\omega_e \sin\left(\theta_e + \frac{2\pi}{3}\right) + \left[i_a\frac{dL_{mca}^{V_1}}{d\theta_e} + i_b\frac{dL_{mcb}^{V_1}}{d\theta_e} + i_c\frac{dL_{sc}^{V_1}}{d\theta_e}\right]\omega_e \tag{15}$$

where V_{dc} is the DC-bus voltage of the inverter. The voltage equations of an IPMSM that uses the second active voltage vector V_2 are shown as the following equations:

$$0.33V_{dc} = r_s i_a + L_{sa}\frac{di_a^{V_2}}{dt} + L_{mab}\frac{di_b^{V_2}}{dt} + L_{mac}\frac{di_c^{V_2}}{dt} - \lambda_m\omega_e \sin\theta_e + \left[i_a\frac{dL_{sa}^{V_2}}{d\theta_e} + i_b\frac{dL_{mab}^{V_2}}{d\theta_e} + i_c\frac{dL_{mac}^{V_2}}{d\theta_e}\right]\omega_e \tag{16}$$

$$0.33V_{dc} = r_s i_b + L_{mba}\frac{di_a^{V_2}}{dt} + L_{sb}\frac{di_b^{V_2}}{dt} + L_{mbc}\frac{di_c^{V_2}}{dt} - \lambda_m\omega_e \sin\left(\theta_e - \frac{2\pi}{3}\right) + \left[i_a\frac{dL_{mba}^{V_2}}{d\theta_e} + i_b\frac{dL_{sb}^{V_2}}{d\theta_e} + i_c\frac{dL_{mbc}^{V_2}}{d\theta_e}\right]\omega_e \tag{17}$$

and

$$-0.67V_{dc} = r_s i_c + L_{mca}\frac{di_a^{V_2}}{dt} + L_{mcb}\frac{di_b^{V_2}}{dt} + L_{sc}\frac{di_c^{V_2}}{dt}$$

TABLE 1. The switching states of inverter.

Voltage Vectors	Switching States			Output Voltages		
	S_a	S_b	S_c	V_a	V_b	V_c
V_1	1	0	0	$0.67V_{dc}$	$-0.33V_{dc}$	$-0.33V_{dc}$
V_2	1	1	0	$0.33V_{dc}$	$0.33V_{dc}$	$-0.67V_{dc}$
V_3	0	1	0	$-0.33V_{dc}$	$0.67V_{dc}$	$-0.33V_{dc}$
V_4	0	1	1	$-0.67V_{dc}$	$0.33V_{dc}$	$0.33V_{dc}$
V_5	0	0	1	$-0.33V_{dc}$	$-0.33V_{dc}$	$0.67V_{dc}$
V_6	1	0	1	$0.33V_{dc}$	$-0.67V_{dc}$	$0.33V_{dc}$
V_0	0	0	0	0	0	0
V_7	1	1	1	0	0	0

$$- \lambda_m \omega_e \sin\left(\theta_e + \frac{2\pi}{3}\right) + \left[i_a \frac{dL_{mca}^{V_2}}{d\theta_e} + i_b \frac{dL_{mcb}^{V_2}}{d\theta_e} + i_c \frac{dL_{sc}^{V_2}}{d\theta_e} \right] \omega_e \quad (18)$$

The voltage equations that use the zero voltage vector V_7 are described as follows:

$$0 = r_s i_a + L_{sa} \frac{di_a^{V_0}}{dt} + L_{mab} \frac{di_b^{V_0}}{dt} + L_{mac} \frac{di_c^{V_0}}{dt} - \lambda_m \omega_e \sin\theta_e + \left[i_a \frac{dL_{sa}^{V_0}}{d\theta_e} + i_b \frac{dL_{mab}^{V_0}}{d\theta_e} + i_c \frac{dL_{mac}^{V_0}}{d\theta_e} \right] \omega_e \quad (19)$$

$$0 = r_s i_b + L_{mba} \frac{di_a^{V_0}}{dt} + L_{sb} \frac{di_b^{V_0}}{dt} + L_{mbc} \frac{di_c^{V_0}}{dt} - \lambda_m \omega_e \sin\left(\theta_e - \frac{2\pi}{3}\right) + \left[i_a \frac{dL_{mba}^{V_0}}{d\theta_e} + i_b \frac{dL_{sb}^{V_0}}{d\theta_e} + i_c \frac{dL_{mbc}^{V_0}}{d\theta_e} \right] \omega_e \quad (20)$$

and

$$0 = r_s i_c + L_{mca} \frac{di_a^{V_0}}{dt} + L_{mcb} \frac{di_b^{V_0}}{dt} + L_{sc} \frac{di_c^{V_0}}{dt} - \lambda_m \omega_e \sin\left(\theta_e + \frac{2\pi}{3}\right) + \left[i_a \frac{dL_{mca}^{V_0}}{d\theta_e} + i_b \frac{dL_{mcb}^{V_0}}{d\theta_e} + i_c \frac{dL_{sc}^{V_0}}{d\theta_e} \right] \omega_e \quad (21)$$

In this paper, a SVPWM-based current-slope sensorless technique is employed to estimate the rotor position. First, the current-slope between the first active voltage vector V_1 and the zero voltage vector V_7 is computed. Then, the current-slope between the second active voltage vector V_2 and the zero voltage vector V_7 is computed. To simplify the method, the resistance drop voltage in V_1, V_2, and V_7 vectors is neglected because the different voltage vectors cancel it out. In addition, in the sampling interval T_s, which is 100 μs, the back-EMF is maintained as a near constant. Furthermore, due to the balance of three-phase currents, the total current-slope in the *a-b-c* phase is equal to zero. By substituting equations (2) to (7) into equations (13) to (21), one can derive the current-slope between the V_1 and V_7 voltage vectors as follows:

$$Di_a^{V_{17}} = \frac{di_a^{V_1}}{dt} - \frac{di_a^{V_7}}{dt} = \frac{V_{dc}\left[\frac{8}{3}L_l + 4L_x + 4L_y\cos(2\theta_e)\right]}{(2L_l + 3L_\Delta)\left(2L_l + 3L_\sum\right)} \quad (22)$$

$$Di_b^{V_{17}} = \frac{di_b^{V_1}}{dt} - \frac{di_b^{V_7}}{dt} = \frac{V_{dc}\left[-\frac{4}{3}L_l - 2L_x - 2L_y\cos(2\theta_e) + 2\sqrt{3}\,L_y\sin(2\theta_e)\right]}{(2L_l + 3L_\Delta)\left(2L_l + 3L_\sum\right)} \quad (23)$$

and

$$0 = \left(\frac{di_a^{V_1}}{dt} - \frac{di_a^{V_7}}{dt}\right) + \left(\frac{di_b^{V_1}}{dt} - \frac{di_b^{V_7}}{dt}\right) + \left(\frac{di_c^{V_1}}{dt} - \frac{di_c^{V_7}}{dt}\right) = Di_a^{V_{17}} + Di_b^{V_{17}} + Di_c^{V_{17}} \quad (24)$$

The current-slope difference between the V_2 and V_7 is shown as follows:

$$Di_a^{V_{27}} = \frac{di_a^{V_2}}{dt} - \frac{di_a^{V_7}}{dt} = \frac{V_{dc}\left[\frac{4}{3}L_l + 2L_x + 2L_y\cos(2\hat{\theta}_e) + 2\sqrt{3}\,L_y\sin(2\theta_e)\right]}{(2L_l + 3L_\Delta)\left(2L_l + 3L_\sum\right)} \quad (25)$$

$$Di_b^{V_{27}} = \frac{di_b^{V_2}}{dt} - \frac{di_b^{V_7}}{dt} = \frac{V_{dc}\left[\frac{4}{3}L_l + 2L_x - 4L_y\cos(2\theta_e)\right]}{(2L_l + 3L_\Delta)\left(2L_l + 3L_\sum\right)} \quad (26)$$

and

$$0 = \left(\frac{di_a^{V_2}}{dt} - \frac{di_a^{V_7}}{dt}\right) + \left(\frac{di_b^{V_2}}{dt} - \frac{di_b^{V_7}}{dt}\right) + \left(\frac{di_c^{V_2}}{dt} - \frac{di_c^{V_7}}{dt}\right) = Di_a^{V_{27}} + Di_b^{V_{27}} + Di_c^{V_{27}} \quad (27)$$

where

$$L_\Delta = L_x - L_y \quad (28)$$

$$L_\sum = L_x + L_y \quad (29)$$

As one can observe in equations (22) to (29), there are two current-slope differences between the two different switching states, and those differences are compensated for by using the zero voltage vector V_7. The aim of this paper is to propose a sensorless technique to estimate the rotor position of the IPMSM, which is inherently included in the current-slope equations in this paper.

The method to calculate the three-phase current-slope is to convert the *a-b-c* axis into the $\alpha - \beta$ axis by using a coordinate transformation. Since there are two current-slopes of two different switching states, a simple rule is proposed here. One can define the following equation:

$$Di_a^{V_{x7}} + Di_b^{V_{x7}} + Di_j^{V_{y7}} \neq 0, \quad \left\{ \begin{array}{c} x \neq y, \forall x, y \in \{1,2,3,4,5,6\} \\ j \in \{a \text{ or } b\} \end{array} \right\} \quad (30)$$

Equation (30) is used to avoid a singularity of the inverse matrix. By using equations (22), (23), and (26) to comply with equation (30), the coordinate transformation of the three-phase current-slopes between the V_1 and V_7 voltage vectors and V_2 and V_7 voltage vectors can be developed as the following equation:

$$\begin{bmatrix} Di_\alpha \\ Di_\beta \\ Di_H \end{bmatrix} = \begin{bmatrix} 4 & 0 & 4 \\ -2 & 2\sqrt{3} & -2 \\ -4 & 0 & 2 \end{bmatrix}^{-1} \begin{bmatrix} Di_a^{V_{17}} \\ Di_b^{V_{17}} \\ Di_b^{V_{27}} \end{bmatrix} \quad (31)$$

From equation (31), we can obtain:

$$Di_\alpha = \frac{V_{dc}L_y\cos(2\theta_e)}{(2L_l+3L_\Delta)(2L_l+3L_\sum)} \tag{32}$$

$$Di_\beta = \frac{V_{dc}L_y\sin(2\theta_e)}{(2L_l+3L_\Delta)(2L_l+3L_\sum)} \tag{33}$$

and

$$Di_H = \frac{V_{dc}\left(\frac{2}{3}L_l+L_x\right)}{(2L_l+3L_\Delta)(2L_l+3L_\sum)} \tag{34}$$

The inverse matrix in equation (31) has different values when different switching states are used. In the real world, the inverse matrix is implemented by using a lookup table technique. Finally, the estimated rotor position is obtained as follows:

$$\theta_e = \frac{\tan^{-1}\left(\frac{Di_\beta}{Di_\alpha}\right)}{2} \tag{35}$$

In equation (35), θ_e is not influenced by the DC input voltage or by the parameters of the IPMSM. In fact, this proposed sensorless technique is very simple because it is only related to Di_α and Di_β. The details of the current-slope sensorless method are depicted in Fig. 1. First, the stator phase-currents are detected and then calculated to obtain the current-slopes. Next, the current-slopes of the a-phase and the b-phase of each switching state can be converted to the $\alpha-\beta$ axis current-slopes. Finally, the rotor position is then easily estimated from equation (35), and the speed is estimated by calculating $\Delta\theta_e/\Delta t$.

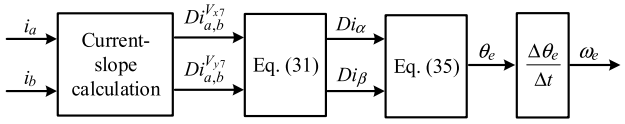

FIGURE 1. Block diagram of the current-slope sensorless technique.

C. CURRENT MEASUREMENT TECHNIQUE

The measurement of stator currents is an essential requirement for current-slope sensorless techniques. The precise detection of the stator currents leads to an accurate estimated rotor position. This paper uses the current-slope between the active voltage vectors and the zero voltage vectors. As a result, two current sampling instances are used for different switching states in every sampling interval. The sampling instance of the first sampling point is 10 μs after the related switch turns on. The sampling instance of the second point is 5 μs before the related switch turns off. Thus, suitable delay time is required to avoid current spikes.

In addition, the current slope measurement is affected by the duration of each switching state. In terms of practicality, a narrow voltage vector is extended to provide sufficient time for stator current detection. The minimum switching time, $T_{\min}$, is set as 20 μs in this paper to ensure the digital signal processor (DSP) has enough time to detect the current slope precisely. Fig. 2 shows the switching pattern and the current sampling diagram when the vector position is in sector 1. If the switching time of the voltage vector V_1 is extended to $T_{\min}$ because it is too narrow, then its opposite vector V_4 is added to compensate for previous extension vector. Once the voltage vector is applied, the corresponding current is measured to compute a precise current-slope by sampling two points in each switching state.

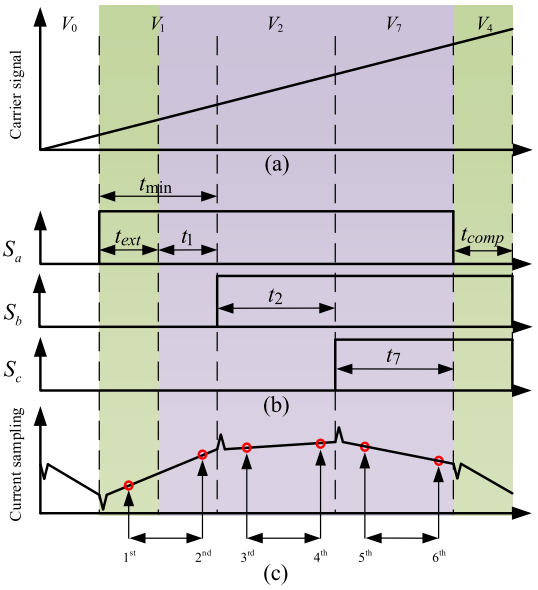

FIGURE 2. Switching pattern and current sampling diagram (a) carrier signal (b) switching states (c) current sampling.

III. PARAMETER ESTIMATION BASED ON CURRENT-SLOPE MEASUREMENTS

As discussed in the previously published papers in [15] to [21], the sensorless and online parameter estimation methods are always two separate methods, and this increases the complexity of the implemented drive system. To solve this problem, this paper proposes a new method that uses current-slope measurements to estimate the d-q axis inductances, magnetic flux, and torque of an IPMSM. The proposed online parameter estimation is executed when the DSP executes the sensorless method; hence, the implementation is achieved in one simple approach without requiring any external high-frequency signal injection or a complicated observer. This is one of the main contributions of this paper. The details are described as follows:

A. INDUCTANCE ESTIMATION

To achieve high-performance sensorless MTPA control, the accurate estimated parameters of the IPMSM are required, such as the estimated parameters L_d, L_q, and λ_m. This paper proposes a current slope-based parameter estimation for an IPMSM, and the details are discussed in this section. From equations (32), (33), and (34), one can obtain the ratio between the estimated inductance L_y and the estimated

inductance $(2/3)L_l + L_x$ as follows:

$$\frac{L_y}{\frac{2}{3}L_l + L_x} = \frac{\sqrt{Di_\alpha^2 + Di_\beta^2}}{Di_H} \tag{36}$$

Then from equation (34), one can obtain:

$$Di_H = \frac{V_{dc}}{9\left(\frac{2}{3}L_l + L_x\right)\left(1 + \left(\frac{L_y}{\frac{2}{3}L_l + L_x}\right)^2\right)} \tag{37}$$

From equations (36) and (37), one can obtain the estimated parameters $(2/3)L_l + L_x$ as follows:

$$\frac{2}{3}L_l + L_x = \frac{V_{dc}}{9Di_H\left(1 - \left(\frac{Di_\alpha^2 + Di_\beta^2}{Di_H^2}\right)\right)} \tag{38}$$

Substituting equation (38) into (37), one can derive the estimated inductance L_y as follows:

$$L_y = \frac{V_{dc}\sqrt{Di_\alpha^2 + Di_\beta^2}}{9Di_H^3\left(1 - \left(\frac{Di_\alpha^2 + Di_\beta^2}{Di_H^2}\right)\right)} \tag{39}$$

Finally, by substituting equations (38) and (39) into equations (8) and (9), the estimated d-axis inductance and the estimated q-axis inductance of the IPMSM can be obtained as the following two equations:

$$L_d = \frac{3}{2}\left(\frac{2}{3}L_l + L_x - L_y\right) \tag{40}$$

and

$$L_q = \frac{3}{2}\left(\frac{2}{3}L_l + L_x + L_y\right) \tag{41}$$

B. MAGNETIC FLUX ESTIMATION

The $\alpha - \beta$ axis voltage equation of an IPMSM is shown as follows:

$$\begin{bmatrix} v_\alpha \\ v_\beta \end{bmatrix} = r_s \begin{bmatrix} i_\alpha \\ i_\beta \end{bmatrix} + L_q \begin{bmatrix} Di_\alpha \\ Di_\beta \end{bmatrix} + \frac{d}{dt}\begin{bmatrix} \lambda_\alpha \\ \lambda_\beta \end{bmatrix} \tag{42}$$

where v_α and v_β are the $\alpha - \beta$ axis voltages. However, in this paper, the voltage commands are used to replace the $\alpha - \beta$ axis stator voltages. In addition, i_α and i_β are the $\alpha - \beta$ axis stator currents and λ_α and λ_β are the $\alpha - \beta$ axis stator flux linkages.

The estimated $\alpha - \beta$ axis flux linkages are expressed as the following two equations:

$$\frac{d\lambda_\alpha}{dt} = v_\alpha - r_s i_\alpha - L_q Di_\alpha = e_\alpha \tag{43}$$

and

$$\frac{d\lambda_\beta}{dt} = v_\beta - r_s i_\beta - L_q Di_\beta = e_\beta \tag{44}$$

The integration of the back EMF is affected by the initial value which is usually unknown and could generate a DC offset. Moreover, in practice, there is a possibility that current detection errors result in some DC offsets and harmonics.

The back EMF signal can be rewritten as a combination of sinusoidal signals as follows [23]:

$$e_s = A_0 + A_f \sin(\omega_f t + \varphi_f) + \sum A_h \sin(\omega_h t + \varphi_h) \tag{45}$$

where e_s is the back EMF vector of the $\alpha - \beta$ axis components. The back EMF in equation (45) has three essential components. A_0 is the dc component, $A_f \sin(\omega_f t + \varphi_f)$ is the fundamental component, and the summation of $A_h \sin(\omega_h t + \varphi_h)$ is the total harmonic component. A_0, A_f, and A_h are the corresponding amplitudes of the signal for each component; ω_f and ω_h are the angular frequencies of the fundamental signal and harmonic signals; and φ_f and φ_h are the initial angles of the fundamental signal and harmonic signals. By taking the Laplace transformation into equation (45), one can obtain the following equation:

$$E_s(s) = \frac{A_0}{s} + A_f \frac{s\sin\varphi_f + \omega_f \cos\varphi_f}{s^2 + \omega_f^2} + \sum A_h \frac{s\sin\varphi_h + \omega_h \cos\varphi_h}{s^2 + \omega_h^2} \tag{46}$$

where s is the Laplace transform operator and $E_s(s)$ is the Laplace transform of e_s. It is a straightforward process to obtain the flux linkage by using an integrator for equation (46). However, the integrator generates a DC offset in the dc component, fundamental signals, and harmonic signals. This DC offset may cause saturation of the estimated flux linkages, and thus, the trajectories drift out of a circular shape. To overcome this problem, a low pass filter (LPF) is applied as a flux linkage estimator and is described as follows:

$$\begin{aligned} \lambda_{s\_LPF} = {} & \frac{A_0}{\omega_e} - \frac{A_0}{\omega_e}e^{-\omega_e t} \\ & + \frac{A_f}{\sqrt{\omega_f^2 + \omega_e^2}} \sin(\omega_f t + \varphi_f - \frac{\pi}{2} + \theta_f) \\ & + \frac{A_f}{\sqrt{\omega_f^2 + \omega_e^2}} \cos(\varphi_f + \theta_f)e^{-\omega_e t} \\ & + \sum \frac{A_h}{\sqrt{\omega_h^2 + \omega_e^2}} \sin(\omega_h t + \varphi_h - \frac{\pi}{2} + \theta_h) \\ & + \sum \frac{A_h}{\sqrt{\omega_h^2 + \omega_e^2}} \cos(\varphi_h + \theta_h)e^{-\omega_e t} \end{aligned} \tag{47}$$

where λ_{s_LPF} is the estimated flux linkage when using an LPF. In (47), the first term of the DC components exponentially decays as the time increases. In addition, the second and third terms of the DC components are affected by their initial values and exponentially decay in steady state. The saturation of the estimated flux linkage, therefore, can be removed. Then, it is not difficult to obtain the estimated permanent magnetic flux as follows:

$$\lambda_m = \sqrt{(\lambda_{\alpha\_LPF})^2 + (\lambda_{\beta\_LPF})^2} \tag{48}$$

The permanent magnetic flux, λ_m, is estimated and then used to compute the estimated torque. The current-slope based

parameter estimation diagram is depicted in Fig. 3. The estimated d-axis inductance, L_d; estimated q-axis inductances, L_q; and estimated magnetic flux of the IPMSM, λ_m, are obtained by using the current-slope detection method.

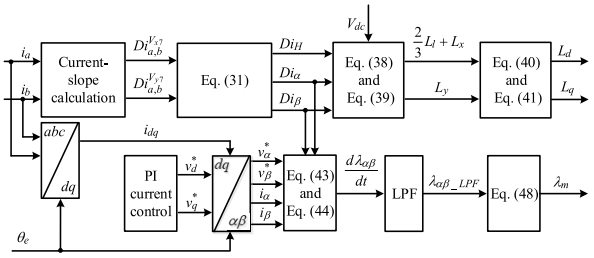

FIGURE 3. Block diagram of the current-slope based parameter estimation.

IV. MTPA AND FLUX-WEAKENING ALGORITHMS

In general, many researchers usually control the IPMSM by setting $i_d = 0$, which can produce linear torque. However, the setting of $i_d = 0$ does not generate reluctance torque. To increase the total torque, a high-performance sensorless IPMSM drive system with real-time MTPA control is proposed in this paper. The MTPA control with online parameter estimation adjusts i_d properly to reach maximum torque. By taking a partial derivative of the estimated torque shown in equation (10) with respect to the i_q, we can obtain the following equation:

$$\frac{\partial T_e}{\partial i_q} = \frac{3P}{4}\left[-(L_d - L_q)\frac{i_q^2}{i_d} + (L_d - L_q)i_d + \lambda_m\right] \quad (49)$$

By setting equation (49) to equal zero, we can derive the following equation:

$$i_d = -\frac{\lambda_m}{2(L_d - L_q)} - \sqrt{\frac{\lambda_m^2}{4(L_d - L_q)^2} + i_q^2} \quad (50)$$

From equation (50), the i_d is adjusted for real-time MTPA control. The accuracy of the i_d is strongly influenced by the estimated parameters of the motor when the MTPA control is executed.

When the speed of the IPMSM increases beyond the nominal speed, a flux weakening algorithm is employed to keep the voltage at a constant. The relationship of the maximum voltage is expressed as the following equation:

$$V_{s\,\max} \geq \sqrt{v_d^2 + v_q^2} \quad (51)$$

where $V_{s\,\max}$ is the maximum phase voltage and is set at $V_{dc}/\sqrt{3}$. In steady state, the d-q axis voltages of the IPMSM are described as the following equation:

$$\begin{bmatrix} v_d \\ v_q \end{bmatrix} = r_s \begin{bmatrix} i_d \\ i_q \end{bmatrix} + \omega_e \begin{bmatrix} -L_q i_d \\ L_d i_d + \lambda_m \end{bmatrix} \quad (52)$$

where v_d is the d-axis voltage and v_q is the q- axis voltage. Substituting equation (51) into (52) and omitting the resistance voltage drops, one can derive the d-axis current as the following equation:

$$i_d = \frac{1}{L_d}\left(-\lambda_m + \sqrt{\left(\frac{V_{s\,\max}}{\omega_e}\right)^2 - \left(L_q i_q\right)^2}\right) \quad (53)$$

From equation (53), real-time flux weakening control of the IPMSM is achieved. The flux weakening control is enabled to decrease the voltage saturation and maintain the maximum phase-voltage as a constant by properly adjusting the d-axis current.

V. EXPERIMENTAL RESULTS

The performance of the proposed method is validated through a bench test in which a rated 500 W, 2000 r/min, 3A, and 4-pole IPMSM is used. The measured parameters of the IPMSM are: $r_s = 1.93\ \Omega$, $L_d = 15$ mH, $L_q = 32$ mH, $\lambda_m = 0.216$ V.s/rad, $J_m = 0.0005$ kg-m^2, and $B_m = 0.003$ N.m.s/rad. The experimental conditions are set as follows:

The DC bus voltage is 200V, the current-loop frequency is 10 kHz and is synchronized with the switching frequency of the inverter, and the speed-loop frequency is 1 kHz.

The implemented drive system is depicted in Fig. 4(a) to (c). Fig.4(a) shows the block diagram of the current-slope sensorless IPMSM drive system with real-time MTPA and flux-weakening control. The phase currents of each switching state are detected for the current-slope calculation. After that, the estimated rotor position as well as the estimated rotor speed are obtained. The estimated parameters L_d, L_q, and λ_m are obtained by using the current-slope. In addition, the estimated parameters, including L_d, L_q, and λ_m are used for real-time MTPA and flux-weakening algorithms. Finally, the closed-loop sensorless IPMSM drive system achieves wide speed-range operations. Fig. 4(b) depicts the hardware circuit which includes a control board with a DSP TMS32F2808, a gate driver board, a three-phase inverter, 16-bit AD converters, and two current sensors. Fig. 4(c) depicts the motor test platform equipped with an external DC load which is installed with a torque sensor to compare the real torque and the estimated torque.

The performance of the proposed current-slope sensorless IPMSM drive system at 1 r/min is shown in Fig. 5(a) to (d). As presented in Fig. 5(a) and (b), the estimated rotor position is obtained within $\pm 2°$ of errors. Fig. 5(c) presents a comparison of the estimated rotor speed and the real rotor speed. Fig. 5(d) shows the estimated speed errors. As can be seen in these figures, the estimated speed errors are ± 0.06 r/min. Fig. 6(a) to (d) demonstrate the current-slope sensorless IPMSM drive system at 2000 r/min. The related $\alpha - \beta$ axis current-slopes which are used for the rotor position estimations are depicted in Fig. 6(a). A comparison of the estimated and the real rotor positions is demonstrated in Fig. 6(b). As one can observe, the rotor position is precisely estimated. Fig. 6(c) presents the estimated position errors, which are $\pm 2°$. Fig. 6(d) presents a comparison of the measured speed responses at 2000 r/min under steady state conditions. Thus, the speed of IPMSM is accurately

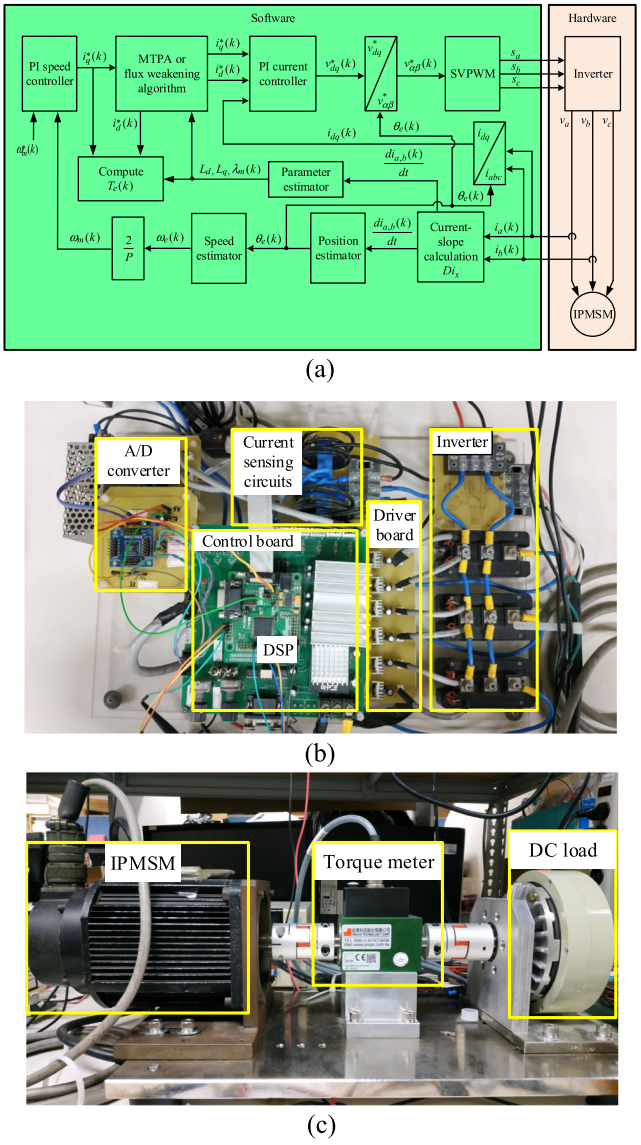

(a)

(b)

(c)

FIGURE 4. Photographs of the implemented drive system (a) block diagram system (b)hardware circuit (c) motor test platform.

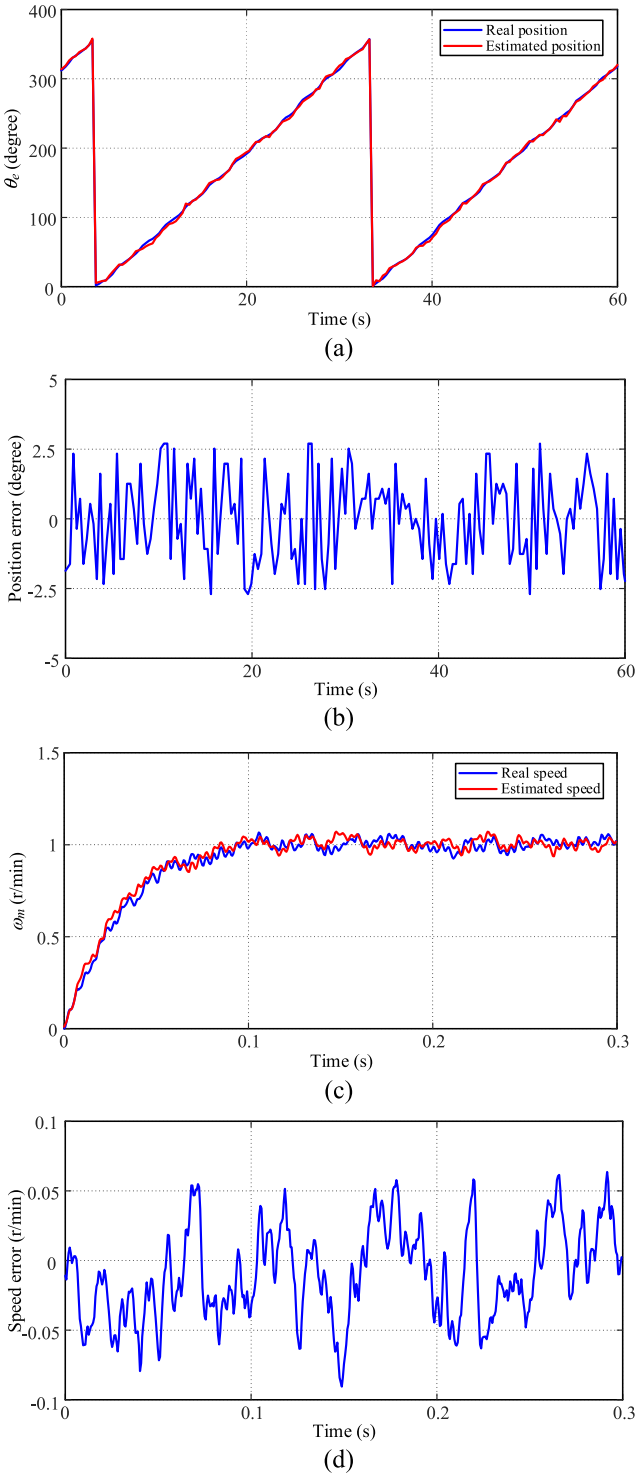

(a)

(b)

(c)

(d)

FIGURE 5. Sensorless response at low speed 1 r/min (a) rotor position (b) position error (c) rotor speed (d) speed errors.

estimated. According to Fig. 5(a) to (d) and Fig. 6(a) to (d), the sensorless IPMSM drive system works well from low speed ranges to the rated speeds.

Fig. 7(a) and (b) show a comparison of the measured L_d and L_q inductances and their related estimated L_d and L_q inductances at different current levels from 0.25 A to the rated current 3A. The estimated inductances are obtained when the IPMSM is operated at 1000 r/min. As one can observe, the estimated inductances match well with the real inductances. Fig. 8(a) and (b) demonstrate the estimated magnetic flux linkages, which include the estimated λ_α and λ_β at 600 r/min. The estimated α-axis flux and β-axis flux and their trajectories are nearly circular. Fig. 8(c) depicts the magnitude of the magnetic flux linkage, which is near 0.22 Wb.

Fig. 9(a) to (c) demonstrate a comparison of real-time MTPA and conventional MTPA control methods with nominal motor parameters during load disturbance tests, from no load to a 2 Nm load at 1000 r/min. In Fig. 9(a), the proposed MTPA with online parameter estimation provides a better load disturbance rejection response, which includes faster recovery times and lower speed drops than conventional

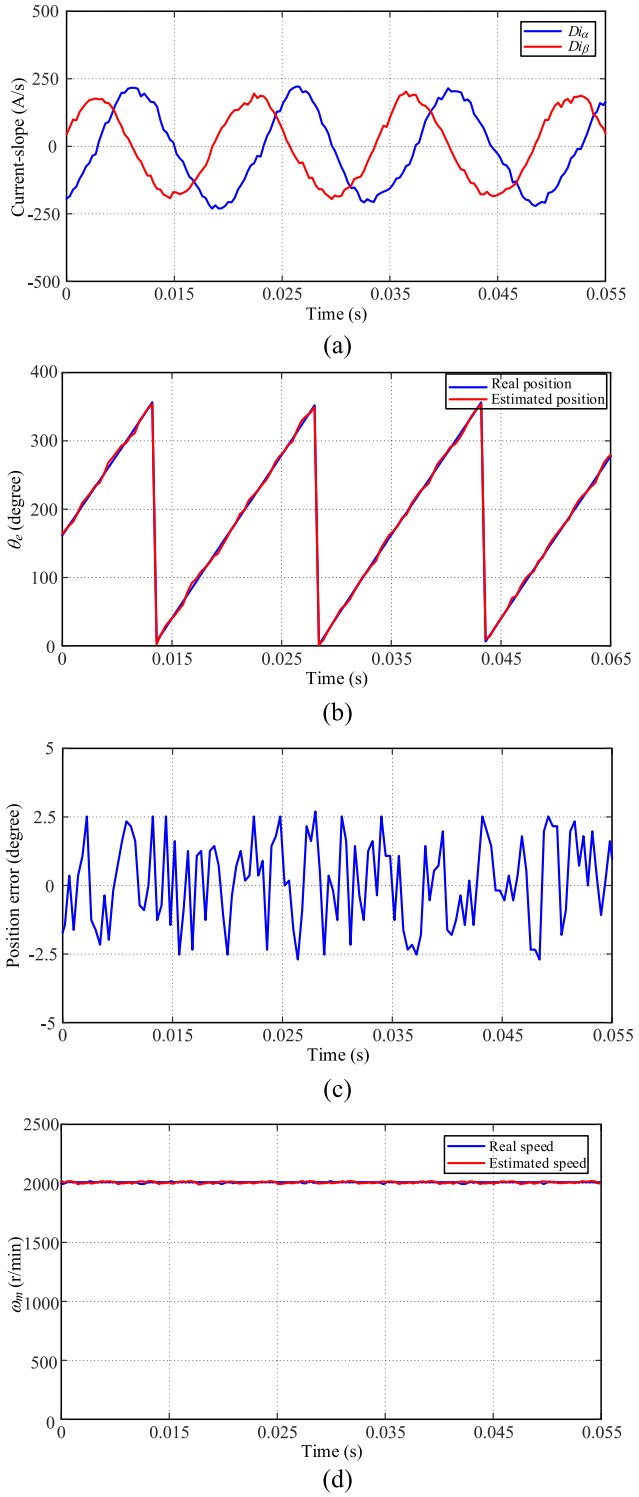

FIGURE 6. Sensorless responses at a nominal speed of 2000 r/min (a) $\alpha - \beta$ current-slope (b) rotor position (c) position error (d) rotor speed.

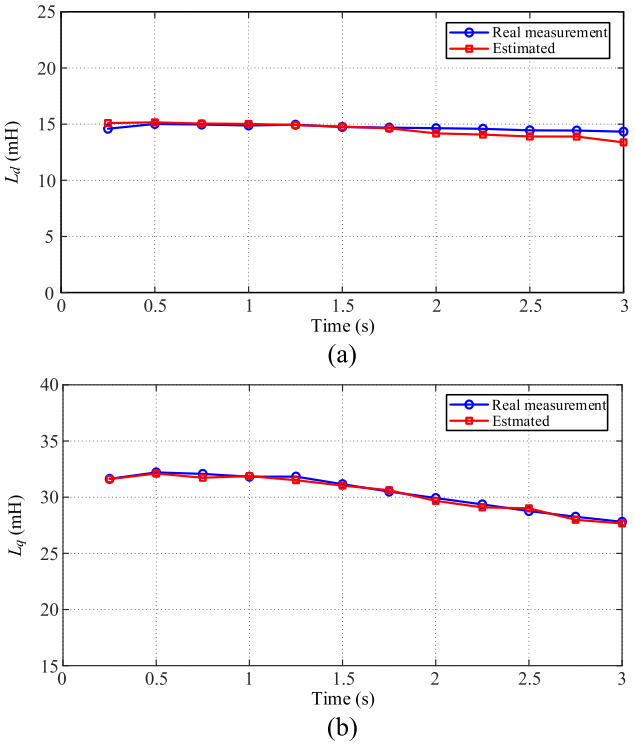

FIGURE 7. Comparison of the measured and estimated inductances (a) d-axis inductance (b) q-axis inductance.

TABLE 2. Comparison of the proposed method and the existing method.

Method	Sensorless Method	Parameter Identification Method	Steady-State Position Error	Adjustable Speed Range
In [15]	Extended back-EMF	Recursive least square	4^o	Below rated speed
In [16]	Adaptive observer with HF signal injection	Adaptive observer with HF signal injection	$\pm 5^o$	Below rated speed
In [17]	Extended back-EMF	Recursive least square	$\pm 9^o$	Below rated speed
In [18]	Adaptive interconnected observer	Adaptive interconnected observer	10^o	Below rated speed
In [19]	Extended back-EMF	Affine projection	$\pm 11.5^o$	1.15 times rated speed
In [20]	Extended back-EMF	Adaptive full-state feedback control	$\pm 4^o$	Rated speed
In [21]	Extended back-EMF	Virtual high-frequency injection	$\pm 6^o$	Below rated speed
Proposed method	Current-slope measurement	Current-slope measurement	$\pm 2.5^o$	1 r/min to 1.5 times over rated speed

MTPA methods with off-line motor parameter measurements. The speed drop of the proposed real-time MTPA is only 18% while a conventional MTPA is 21.8%. A comparison of the d-q axis currents is depicted in Fig. 9(b). When the load increases from no load to a 2 Nm load, the q-axis current increases from 0.25A to 3A, and the d-axis current changes to a negative current to achieve higher total torque. By using this proposed method, the d-axis current has a smaller current ripple compared to conventional MTPAs. Fig. 9(c) presents

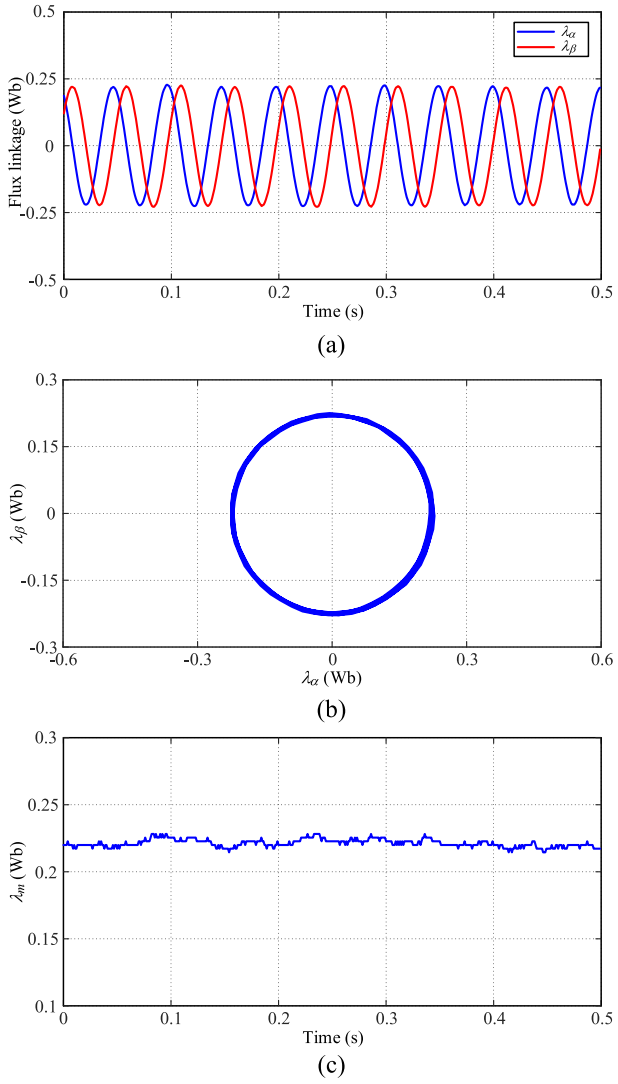

FIGURE 8. Estimated permanent magnet flux at 600 r/min (a) estimated $\alpha - \beta$ flux linkages (b) flux linkage trajectory (c) magnetic flux constant.

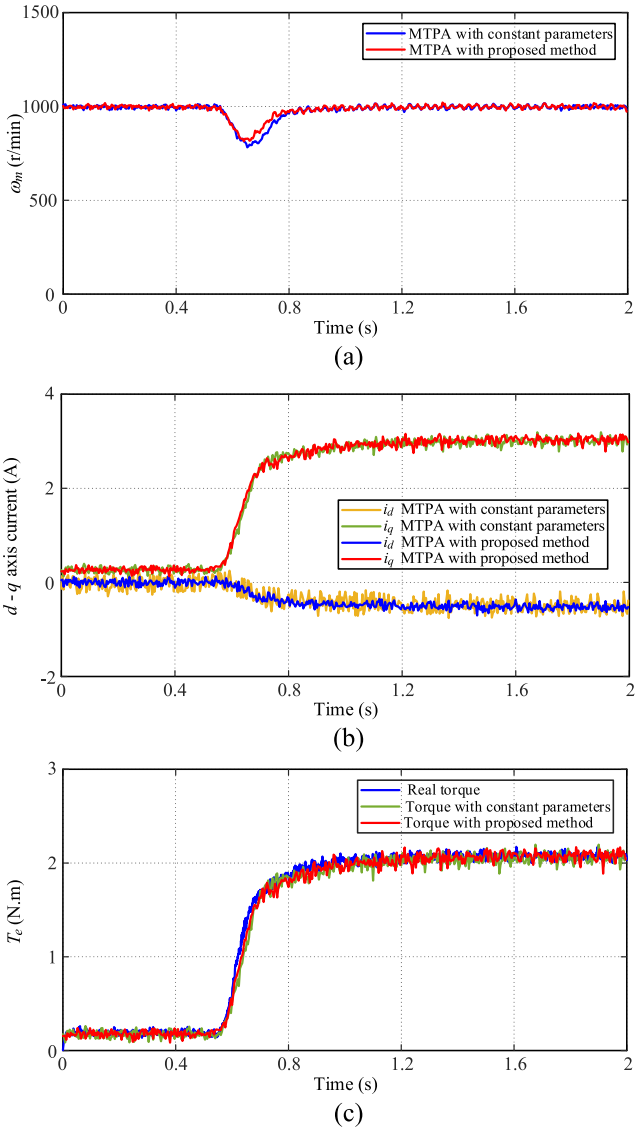

FIGURE 9. Comparison of load disturbance responses at 1000 r/min between a real-time MTPA and a conventional MTPA (a) speed responses (b) d-q axis currents (c) torque.

a comparison of the real torque T_e that uses a torque sensor, the estimated torque T_e of a conventional MTPA using off-line parameter estimation, and the estimated torque T_e of the proposed MTPA with online parameter estimation. As one can observe, the proposed real-time MTPA has better torque tracking ability when compared to a conventional MTPA. Fig 10(a) to (c) demonstrate the performance of the proposed flux-weakening control and the conventional flux-weakening control when the motor is operated from standstill to 3000 r/min with a 1.5 Nm load. Fig 10(a) to (c) also include the estimated rotor speeds, d-q axis currents, and current trajectories respectively. When the speed of the IPMSM goes beyond the base-speed, the d-axis current is decreased to achieve flux-weakening control. As one can observe, the real-time flux-weakening can effectively reduce the d-axis flux when compared to conventional flux-weakening control. As a result, the performance of the real-time flux-weakening control achieves a higher speed than conventional flux-weakening control.

Fig. 11(a) and (b) and Fig. 12(a) and (b) show the performance of the tracking capabilities of the proposed method with various speed commands from standstill to 1500 r/min, as well as reversed to -1500 r/min. Fig. 11(a) presents the rotor position responses at a reversing speed command. The rotor position is precisely estimated although the speed command is suddenly reversed. Fig. 11(b) presents the speed responses of a reversing speed command. As depicted in those figures, the proposed method determines a satisfactory rotor position and speed estimation. Fig. 12(a) and (b) demonstrate the varied speed commands including a trapezoidal command and a triangular command, both of which have satisfactory

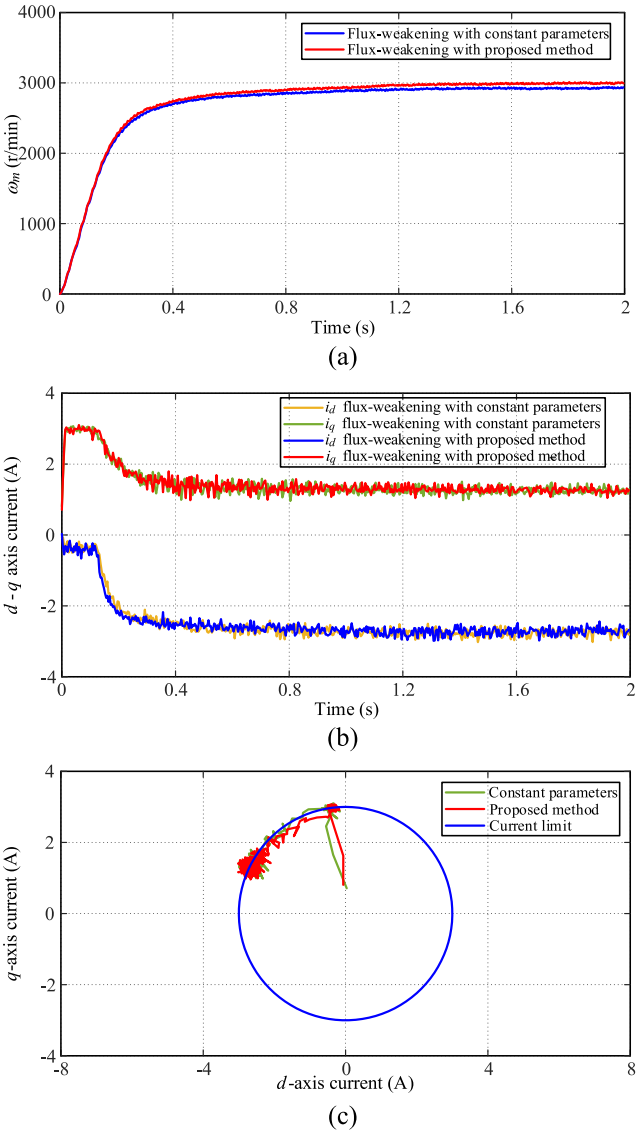

FIGURE 10. Responses of the extended speed at 3000 r/min between the proposed method and conventional flux-weakening (a) speed responses (b) d-q axis currents (c) current trajectories.

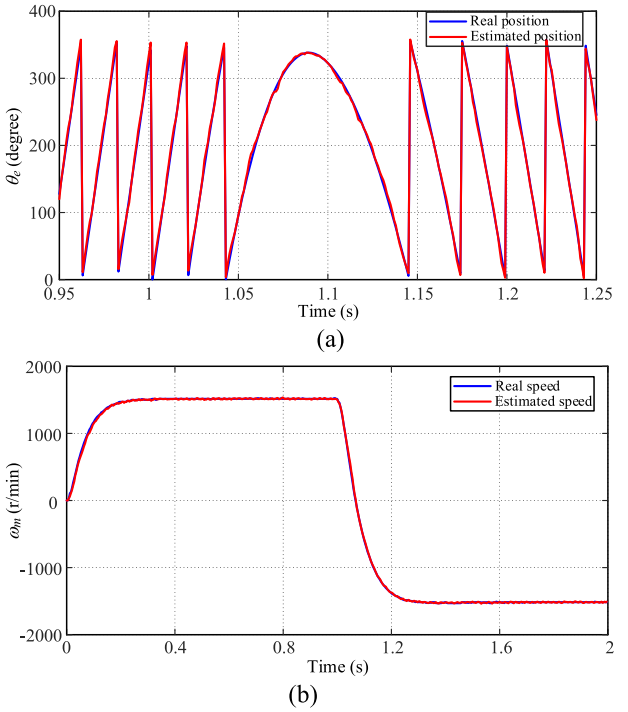

FIGURE 11. Responses of the reverse speed command at 1500 r/min (a) rotor position (b) rotor speed.

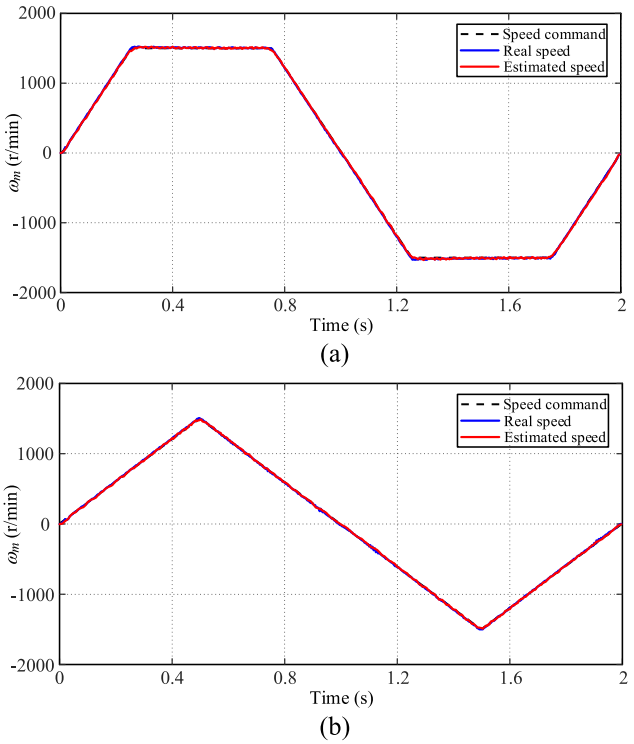

FIGURE 12. Different speed responses of time-varying commands (a) trapezoidal (b) triangular.

tracking responses. These results confirm that the proposed sensorless drive system provides good tracking ability.

From the measured results, it is possible to compare the proposed method with previosly published methods to show the effectiveness of the provided method. Table 2 shows a comparison of the proposed method and methods proposed in previously published papers. As we can observe in references [15] to [21], those papers used different approaches for their sensorless methods and parameter identification methods. The complexity and the computational burden on the DSP became a neccessity that had to be compensated for. In contrast, the proposed method in this paper uses only current-slope measurements for sensorless and parameter identification. As a result, the proposed method in this paper is simpler and easier than the methods published in [15] to [21]. In addition, the rotor position errors are slight and are wihtin $\pm 2.5°$. Furthermore, a wide adjustable speed range from 1 r/min to 1.5 times over the rated speed is achieved, which are better results than the methods published in [15] to [21].

VI. CONCLUSION

A sensorless IPMSM drive and an online parameter estimation method based on current-slope measurements are proposed and implemented in this paper. The proposed drive system achieves rotor position estimation and online parameter estimation by measuring the slope of three-phase stator currents. The rotor position, rotor speed, *d-q* axis inductances, and permanent-magnet flux are precisely estimated without using any external high-frequency signal injection or a complicated observer. Moreover, the proposed sensorless drive system is operated with real-time MTPA and flux-weakening control. Experimental results confirm that this proposed sensorless IPMSM drive system achieves a wide adjustable speed range from 1 r/min to 3000 r/min with satisfactory performance, including estimated position errors of only $\pm 2.5°$, good dynamic responses, and good tracking responses. To further improve the dynamic responses, further studies could use advanced controllers such as sliding mode controllers in [24] to [25] or model predictive controllers in [26] to replace the proposed PI controllers.

REFERENCES

[1] G. Pellegrino, A. Vagati, B. Boazzo, and P. Guglielmi, "Comparison of induction and PM synchronous motor drives for EV application including design examples," *IEEE Trans. Ind. Appl.*, vol. 48, no. 6, pp. 2322–2332, Nov./Dec. 2012.
[2] Z. Yang, F. Shang, I. P. Brown, and M. Krishnamurthy, "Comparative study of interior permanent magnet, induction, and switched reluctance motor drives for EV and HEV applications," *IEEE Trans. Transport. Electrific.*, vol. 1, no. 3, pp. 245–254, Oct. 2015.
[3] S. Medjmadj, D. Diallo, M. Mostefai, C. Delpha, and A. Arias, "PMSM drive position estimation: Contribution to the high-frequency injection voltage selection issue," *IEEE Trans. Energy Convers.*, vol. 30, no. 1, pp. 349–358, Mar. 2015.
[4] J. Lu, Y. Hu, X. Zhang, Z. Wang, J. Liu, and C. Gan, "High-frequency voltage injection sensorless control technique for IPMSMs fed by a three-phase four-switch inverter with a single current sensor," *IEEE/ASME Trans. Mechatronics*, vol. 23, no. 2, pp. 758–768, Apr. 2018.
[5] F. Genduso, R. Miceli, C. Rando, and G. R. Galluzzo, "Back EMF sensorless-control algorithm for high-dynamic performance PMSM," *IEEE Trans. Ind. Electron.*, vol. 57, no. 6, pp. 2092–2100, Jun. 2010.
[6] A. T. Woldegiorgis, X. Ge, S. Li, and M. Hassan, "Extended sliding mode disturbance observer-based sensorless control of IPMSM for medium and high-speed range considering railway application," *IEEE Access*, vol. 7, pp. 175302–175312, 2019.
[7] M.-Y. Wei and T.-H. Liu, "A high-performance sensorless position control system of a synchronous reluctance motor using dual current-slope estimating technique," *IEEE Trans. Ind. Electron.*, vol. 59, no. 9, pp. 3411–3426, Sep. 2012.
[8] X. Luo, Q. Tang, A. Shen, H. Shen, and J. Xu, "A combining FPE and additional test vectors hybrid strategy for IPMSM sensorless control," *IEEE Trans. Power Electron.*, vol. 33, no. 7, pp. 6104–6113, Jul. 2018.
[9] A. Vogelsberger, S. Grubic, T. G. Habetler, and T. M. Wolbank, "Using PWM-induced transient excitation and advanced signal processing for zero-speed sensorless control of AC machines," *IEEE Trans. Ind. Electron.*, vol. 57, no. 1, pp. 365–374, Jan. 2010.
[10] S. K. Tseng, T. H. Liu, and J. L. Chen, "Implementation of a sensorless interior permanent magnet synchronous drive based on current deviations of pulse-width modulation switching," *IET Electr. Power Appl.*, vol. 9, no. 2, pp. 95–106, Mar. 2015.
[11] Y. Hua, M. Sumner, G. Asher, Q. Gao, and K. Saleh, "Improved sensorless control of a permanent magnet machine using fundamental pulse width modulation excitation," *IET Electr. Power Appl.*, vol. 5, no. 4, pp. 359–370, Apr. 2011.
[12] M. X. Bui, D. Guan, D. Xiao, and M. F. Rahman, "A modified sensorless control scheme for interior permanent magnet synchronous motor over zero to rated speed range using current derivative measurements," *IEEE Trans. Ind. Electron.*, vol. 66, no. 1, pp. 102–113, Jan. 2019.
[13] C. Wu, Z. Chen, and Q. Chen, "An optimized asymmetric pulsewidth modulation for sensorless control of permanent magnet synchronous machines," *IEEE Trans. Ind. Electron.*, vol. 69, no. 2, pp. 1389–1399, Feb. 2022.
[14] S. Morimoto, M. Sanada, and Y. Takeda, "Mechanical sensorless drives of IPMSM with online parameter identification," *IEEE Trans. Ind. Appl.*, vol. 42, no. 5, pp. 1241–1248, Sep./Oct. 2006.
[15] S. Ichikawa, M. Tomita, S. Doki, and S. Okuma, "Sensorless control of permanent-magnet synchronous motors using online parameter identification based on system identification theory," *IEEE Trans. Ind. Electron.*, vol. 53, no. 2, pp. 363–372, Apr. 2006.
[16] A. Piippo, M. Hinkkanen, and J. Luomi, "Adaptation of motor parameters in sensorless PMSM drives," *IEEE Trans. Ind. Appl.*, vol. 45, no. 1, pp. 203–212, Jan./Feb. 2009.
[17] Y. Inoue, Y. Kawaguchi, S. Morimoto, and M. Sanada, "Performance improvement of sensorless IPMSM drives in a low-speed region using online parameter identification," *IEEE Trans. Ind. Appl.*, vol. 47, no. 2, pp. 798–804, Mar. 2011.
[18] M. A. Hamida, J. De Leon, A. Glumineau, and R. Boisliveau, "An adaptive interconnected observer for sensorless control of PM synchronous motors with online parameter identification," *IEEE Trans. Ind. Electron.*, vol. 60, no. 2, pp. 739–748, Feb. 2013.
[19] M. S. Rafaq, F. Mwasilu, J. Kim, H. H. Choi, and J.-W. Jung, "Online parameter identification for model-based sensorless control of interior permanent magnet synchronous machine," *IEEE Trans. Power Electron.*, vol. 32, no. 6, pp. 4631–4643, Jun. 2017.
[20] Y. Yao, Y. Huang, F. Peng, and J. Dong, "Position sensorless drive and online parameter estimation for surface-mounted PMSMs based on adaptive full-state feedback control," *IEEE Trans. Power Electron.*, vol. 35, no. 7, pp. 7341–7355, Jul. 2020.
[21] Q. Tang, A. Shen, P. Luo, H. Shen, W. Li, and X. He, "IPMSMs sensorless MTPA control based on virtual *q*-axis inductance by using virtual high-frequency signal injection," *IEEE Trans. Ind. Electron.*, vol. 67, no. 1, pp. 136–146, Jan. 2020.
[22] C.-K. Liu, T.-H. Lo, and C.-H. Lo, "Sensorless interior permanent magnet synchronous motor drive system with a wide adjustable speed range," *IET Electr. Power Appl.*, vol. 3, no. 2, pp. 133–146. Mar. 2009.
[23] W. Xu, Y. Jiang, C. Mu, and F. Blaabjerg, "Improved nonlinear flux observer-based second-order SOIFO for PMSM sensorless control," *IEEE Trans. Power Electron.*, vol. 34, no. 1, pp. 565–579, Jan. 2019.
[24] B. Xu, L. Zhang, and W. Ji, "Improved non-singular fast terminal sliding mode control with disturbance observer for PMSM drives," *IEEE Trans. Transport. Electrific.*, vol. 7, no. 4, pp. 2753–2762, Dec. 2021.
[25] L. Liu, S. Ding, and X. Yu, "Second-order sliding mode control design subject to an asymmetric output constraint," *IEEE Trans. Circuits Syst. II, Exp. Briefs*, vol. 68, no. 4, pp. 1278–1282, Apr. 2021.
[26] T. Tarczewski and L. M. Grzesiak, "Constrained state feedback speed control of PMSM based on model predictive approach," *IEEE Trans. Ind. Electron.*, vol. 63, no. 6, pp. 3867–3875, Jun. 2016.

MUHAMMAD SYAHRIL MUBAROK (Graduate Student Member, IEEE) received the B.S. degree in electrical engineering from the Electronic Engineering Polytechnic Institute of Surabaya, Surabaya, Indonesia, in 2015, and the M.S. degree in electrical engineering from the National Taiwan University of Science and Technology, Taipei, Taiwan, in 2018, where he is currently pursuing the Ph.D. degree.

His research interests include electric motor drive systems, sensorless techniques, and model predictive control.

TIAN-HUA LIU (Life Fellow, IEEE) received the B.S., M.S., and Ph.D. degrees from the National Taiwan University of Science and Technology (NTUST), Taiwan.

He is currently a Distinguished Professor at NTUST. His research interest includes motor controls. He was an Associate Editor of IEEE TRANSACTIONS ON INDUSTRIAL ELECTRONICS. He is currently an Associate Editor of *IET Electric Power Applications*.